Int. J. Solids Structures Vol. 30, No. 10, pp. 1379–1395, 1993
Printed in Great Britain

0020-7683/93 $6.00+ .00

THE EFFECT OF INTERFACIAL FRICTION ON THE BUCKLE-DRIVEN SPONTANEOUS DELAMINATION OF A COMPRESSED THIN FILM

R. G. STRINGFELLOW† and L. B. FREUND
Division of Engineering, Brown University, Providence, RI, U.S.A.

(*Received* 18 *July* 1991; *in revised form* 1 *October* 1992)

Abstract—We consider the process of frictional interaction during the delamination of a compressed thin film from a substrate in order to assess the effect of Coulomb friction on the energy release rate, G, driving the delamination. For the case in which the film and the substrate have identical elastic properties, we derive a singular integral equation for the relative sliding displacement of the opposing faces of the debonded interface. Using an analytical model, we find that G decreases by about 35% when the coefficient of interfacial friction is equal to one. Using finite element methods, we then investigate the effects of compliance differences between the film and the substrate, as well as the bending that arises during the post-buckling response of the film. We find that, when the film is more compliant than the substrate, frictional interaction is enhanced and the calculated energy release rate decreases substantially. We further find that, when bending forces are taken into account, G is significantly affected only when the ratio of the length of the delamination to the thickness of the film is relatively small. We conclude that frictional effects can be significant in reducing the delamination driving force, and they can play an important role in the observed arrest of spreading delaminations.

1. INTRODUCTION

The mechanical behavior of thin films is currently a topic of interest in the micro-electronics industry. In film/substrate systems, mechanical strains that are incompatible with a stress-free state are introduced unintentionally during fabrication. In particular, the film is often vapor-deposited onto the substrate at high temperature and, upon cooling, a mismatch strain arises from the differences between the coefficients of thermal expansion of the film and the substrate. As the substrate is much more massive than the film, it contracts freely and imposes a strain, ε_0, on the film in all directions parallel to the interfacial plane. While this strain may be tensile or compressive, depending on material properties, attention here is focussed on the case of compression. The corresponding residual compressive stress, σ_0, can lead to failure modes in which the film decoheres from the substrate. The film first buckles in some small region where adhesion between film and substrate is poor. The post-buckling behavior of the film loads the edge of the newly-formed interfacial crack, causing it to spread (Evans and Hutchinson, 1984). The subsequent fracture behavior is mixed mode, and it has been shown (Whitcomb, 1986) that, as the buckle spreads, the stress state tends toward mode II. It is commonly observed that the buckles do not continue to spread under the constant residual stress, σ_0. Instead, arrest of the propagating crack occurs when the buckle has reached some characteristic dimension. It is generally argued that crack arrest occurs because interfacial fracture toughness is *intrinsically* higher in mode II than in mode I, as evidenced by the observed relationship between interface toughness Γ and phase angle $\psi = \tan^{-1}(K_{II}/K_I)$ (where K_I and K_{II} are the mode I and mode II stress intensity factors), as shown schematically by the solid curve in Fig. 1. In reference to this figure, the values of K_I and K_{II} are normally viewed as local field scaling parameters. In this case, however, these values are understood to be only *apparent* stress intensity factors whose values are determined by remote loads. With this understanding, phase angles less than $-90°$ are acceptable, but angles in this range are actually associated with interpenetration of the film and the substrate, and imply the existence of contact forces which preclude such deformations. No matter what the interpretation of K_I and K_{II}, crack arrest is presumed to

† Current address: Arthur D. Little, Inc., Cambridge, MA, U.S.A.

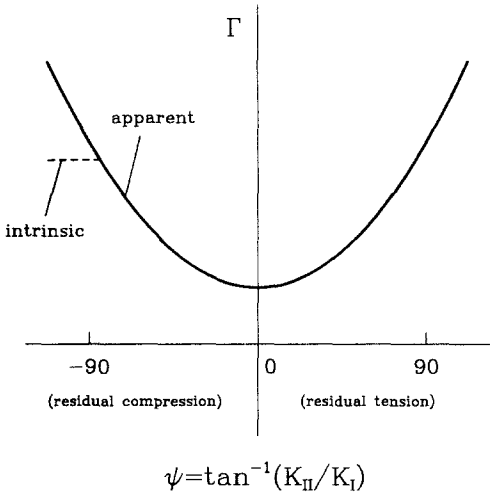

Fig. 1. A diagram showing interface toughness, Γ, versus phase angle, $\psi = \tan^{-1}(K_{II}/K_I)$. K_I and K_{II} are understood to be apparent stress intensity factors determined by remote loads, so that negative values of K_I are acceptable. The solid line represents the apparent toughness, and the dashed line represents "intrinsic" toughness, i.e. that part not attributable to frictional resistance. We assume in this figure that negative values of ψ correspond to residual compression while positive values are associated with residual tension.

occur when the decreasing phase angle ψ reaches a value for which the fracture toughness exceeds the force driving the crack, which remains relatively constant.

One aspect of the thin film delamination problem which has received little attention is the frictional sliding which accompanies crack propagation. As the buckle spreads, the post-buckling response of the film tends to drive it into the substrate near the end of the delamination. Frictional interference between the film and the substrate in this region may be significant in screening the delamination front from the applied loading. It can thus be argued that the apparent increase in interfacial fracture resistance accompanying the decrease in phase angle below $\psi = -90°$ may be the result of frictional resistance. This leads us to the interpretation given by the dashed line shown in Fig. 1, which differentiates between *apparent* and *intrinsic* measures of interface toughness.

In order to quantitatively assess the significance of friction, we study the problem of a plane strain interfacial crack between a film and a substrate. We assume that the residual stress, σ_0, is not too large, so that most of the body remains in the elastic regime. Near each crack tip, we assume there exists an interfacial region, separating the fully bonded interface and the fully separated buckle, within which the film/substrate interaction is governed by Coulomb friction (Fig. 2).

Both analytical and computational approaches are used. We use an analytical method for the case in which the film and the substrate have identical elastic, isotropic properties. We then perform finite element calculations in order to evaluate the effects of friction for systems with more complex features, using the analytical solution as check on the computational approach. We first perform numerical calculations for the same problem that we have solved analytically and compare the results obtained using the two methods, and then extend our numerical analysis to consider problems in which the elastic properties of the film and substrate are different. Finally, we consider a more realistic scenario in which we account for the post-buckling bending moment and in-plane force, whose magnitudes become significant relative to σ_0 when the ratio of the half-length of the delaminated region to the film thickness, b/h, is small.

2. ANALYTICAL MODEL

In this section we develop an accurate model for the case in which the film and substrate have identical properties, so that the film is simply a surface layer of a planar body. We

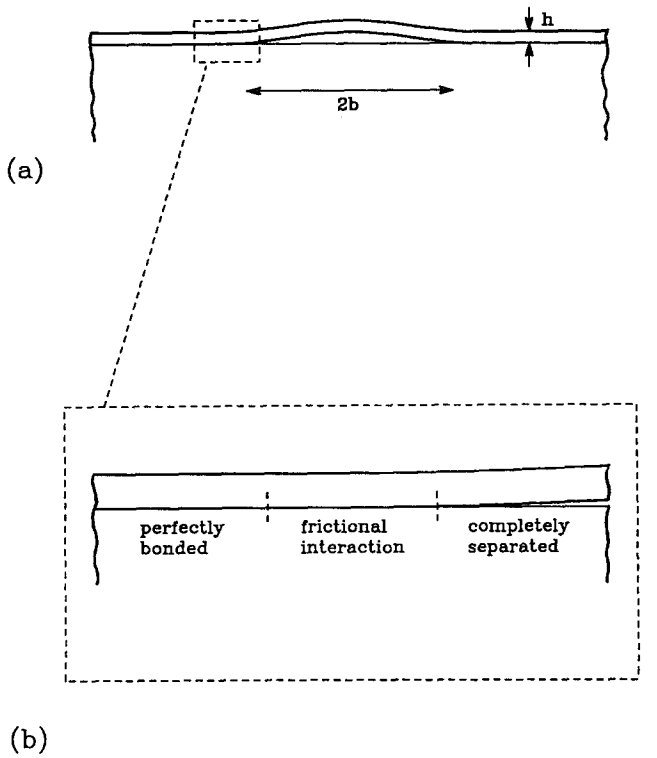

Fig. 2. A diagram of the delamination process in a planar film/substrate system. (a) A film of thickness h, which has delaminated from the substrate, forming a buckle of length $2b$. (b) The region near the leading edge of the delamination, which can be separated into the three indicated regimes.

consider the case of spontaneous delamination, that is, the mismatch strain is so large that, if a delamination is nucleated, it will propagate without an externally applied driving force. We assume that the length of the buckled delamination, $2b$, is large compared to the thickness, h, of the film, so that h is the only relevant length scale in the problem (see Fig. 2). Under this assumption the moment and in-plane forces arising during the post-buckling response of the film become negligible. We assume that the delamination undergoes steady-state propagation, so that all relevant kinematical quantities are measured with respect to the steadily moving crack tip. Since frictional processes are localized around the leading edge of the delamination, we focus attention on this region, far away from the ends of the film.

We therefore model this system as a two-dimensional elastic half-space containing a thin layer of material adjacent to the free surface (the film), which is uniformly compressed far ahead of the delamination front and perfectly bonded to the substrate along one-half of its infinite length but which has debonded along the other half of its length, and thus is stress free far behind the delamination front, as shown in Fig. 3(a). Using the principle of superposition, we separate this problem into two equivalent ones, as shown in Figs 3(b) and 3(c). In the problem of Fig. 3(b), the misfit strain arising from residual compression is balanced by a mechanical strain corresponding to a compressive stress remotely applied to the decohered part of the layer. To recover the original problem, we superpose a remote *tensile* stress [Fig. 3(c)] which balances the compressive end stress of Fig. 3(b). In this problem, however, there is no misfit strain. The solution to the problem of Fig. 3(b) is immediate; the film is in a state of uniform compression and the remainder of the half-space (the substrate) is unstressed. We thus need only solve the problem depicted in Fig. 3(c), which lends itself to an analytical approach.

At the debonded film/substrate interface, we assume that the film is free to slide along the substrate. Therefore, interfacial shear stresses can develop only through frictional effects

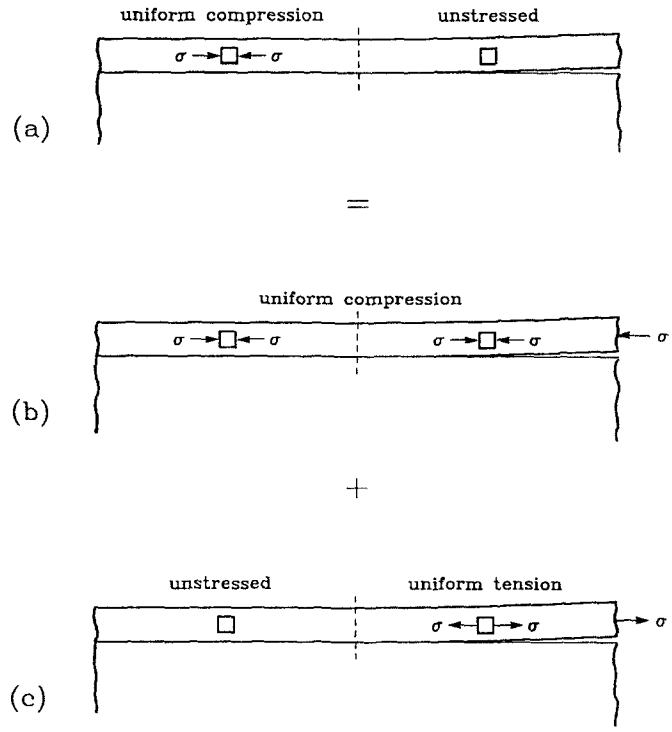

Fig. 3. A diagram of the superposition scheme. (a) The problem that we wish to solve. A film, resting on a massive substrate, is subjected to uniform compression to the left of the interfacial crack tip, but unstressed to the right of the crack tip. This problem is separated into two equivalent ones: (b) uniform compression in the film, and (c) a tensile remote force acting to the right of the crack tip, with the left of the crack tip unstressed.

arising from compressive contact. To simplify the problem, we further assume that the crack faces are in contact along their entire length. The implications of this approximation are discussed below.

Following an idea which appears to have been first suggested by Liebfried (1951), we model the unbonded portion of the interface using a continuous distribution of Volterra elastic dislocations. The fundamental building block for such a distribution is the stress field arising from a *single*, isolated dislocation. The elastic stress field for a single edge dislocation with Burger's vector $\{b_x, b_y, 0\}$ situated a distance h below a free surface (Fig. 4), can be derived from the following Airy stress function (Head, 1953; Dundurs, 1969):

$$\Phi = \frac{\mu}{4\pi(1-\nu)}\left\{\frac{2b_y hx(h-y)+b_x h[x^2+(2h-y)y]}{x^2+(2h-y)^2}+\frac{1}{2}(b_y x-b_x y)\log\left[\frac{x^2+y^2}{x^2+(2h-y)^2}\right]\right\}. \tag{1}$$

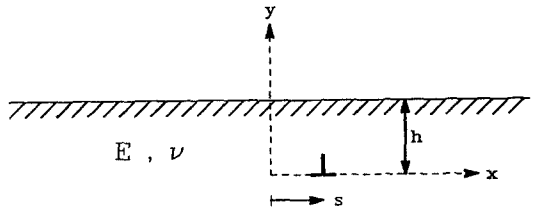

Fig. 4. A diagram of the coordinate system for an elastic edge dislocation situated a distance h below a free surface at x-axis location s.

The relevant stress components along the x-axis for a single dislocation located at $x = s$ are thus given as

$$\sigma_{xy}(x) = -\frac{\partial^2 \Phi}{\partial x\,\partial y} = \frac{\mu}{4\pi(1-\nu)}\left(\frac{g_{11}(\xi)}{\xi}b_x + g_{12}(\xi)b_y\right), \tag{2}$$

$$\sigma_{yy}(x) = \frac{\partial^2 \Phi}{\partial x^2} = \frac{\mu}{4\pi(1-\nu)}\left(g_{21}(\xi)b_x + \frac{g_{22}(\xi)}{\xi}b_y\right), \tag{3}$$

where $\xi = x - s$ and

$$g_{11}(\xi) = \frac{64h^6 + 16h^4\xi^2 + 16h^2\xi^4}{(4h^2+\xi^2)^3}, \tag{4}$$

$$g_{12}(\xi) = \frac{-32h^5 + 24h^3\xi^2}{(4h^2+\xi^2)^3}, \tag{5}$$

$$g_{21}(\xi) = \frac{32h^5 - 24h^3\xi^2}{(4h^2+\xi^2)^3}, \tag{6}$$

$$g_{22}(\xi) = \frac{64h^6 - 48h^4\xi^2}{(4h^2+\xi^2)^3}. \tag{7}$$

Note that σ_{yy} and σ_{xy} are singular along the dislocation line, $x = s$.

We can generalize the stress fields given above from the case of a single, isolated dislocation with finite Burger's vector to the case of a continuous distribution of dislocations with infinitesimal Burger's vectors simply by letting

$$b_x \to \beta_x(s)\,ds \quad \text{and} \quad b_y \to \beta_y(s)\,ds, \tag{8}$$

where $\beta_x(s)$ and $\beta_y(s)$ represent the x- and y-components of the *dislocation density* at s. These are related to the x- and y-components of the x-axis displacements, u_x and u_y, according to

$$\beta_x(s) = u_x(s, 0^+) - u_x(s, 0^-), \tag{9}$$

$$\beta_y(s) = u_y(s, 0^+) - u_y(s, 0^-). \tag{10}$$

By allowing the arclength s to vary from 0 to ∞ on the x-axis, the stress components for a continuous distribution of dislocations with density components $\beta_x(s)$ and $\beta_y(s)$, are thus

$$\sigma_{xy}(x) = \frac{\mu}{4\pi(1-\nu)}\left[\int_0^\infty \frac{g_{11}(\xi)}{\xi}\beta_x(s)\,ds + \int_0^\infty g_{12}(\xi)\beta_y(s)\,ds\right], \tag{11}$$

$$\sigma_{yy}(x) = \frac{\mu}{4\pi(1-\nu)}\left[\int_0^\infty g_{21}(\xi)\beta_x(s)\,ds + \int_0^\infty \frac{g_{22}(\xi)}{\xi}\beta_y(s)\,ds\right], \tag{12}$$

where the singular integrals are interpreted in the sense of Cauchy principal value integrals.

If we wish to study the crack problem in which the remote load is compressive, the conditions $\sigma_{yy}(x) = \sigma_{xy}(x) = 0$, $x > 0$ yield integral equations for β_x and β_y. This problem has been previously solved by Thouless *et al.* (1987).

If, on the other hand, the end force is *tensile*, as it is for the problem that we have proposed to solve [Fig. 3(c)], then the crack faces will come into contact along some portion

of their length, and there can be no condition imposed upon σ_{yy} within this part of the domain. The boundary conditions for this region arise through enforcement of the frictional sliding condition

$$\sigma_{xy} = \begin{cases} -\mu_f \sigma_{yy} & \sigma_{yy} < 0, \\ 0 & \sigma_{yy} = 0. \end{cases} \tag{13}$$

As noted above, to facilitate a solution of this problem, we assume that the crack faces are in contact along the *entire length* of the interface, so that $\beta_y(x) = 0$ from (10), and we solve the following singular integral equation to find the unknown density function β_x,

$$\int_0^\infty \frac{g_{11}(\xi)}{\xi} \beta_x(s)\, ds = -\mu_f \int_0^\infty g_{21}(\xi)\beta_x(s)\, ds. \tag{14}$$

Far away from the crack tip, the film is in a uniform state of plane strain extension with a prescribed tension $\sigma_0 = E'\varepsilon_0$, where $E' = E/(1-\nu^2)$, so that

$$\lim_{x\to\infty} \beta_x \to \varepsilon_0 \quad \text{or} \quad \lim_{x\to\infty} \frac{\beta_x}{\varepsilon_0} \to 1. \tag{15}$$

Approaching the crack tip, the strain, and thus the dislocation density, exhibits a square root singularity, so that

$$\lim_{x\to 0} \beta_x \propto \frac{1}{\sqrt{x}}. \tag{16}$$

Since we have assumed *a priori* that $\beta_y = 0$, an exact solution of this equation requires that $\sigma_{yy} \leqslant 0$ for all $x > 0$. We formulate an approximate solution by neglecting any contribution to the right-hand side of (14) from tensile normal stresses. This solution can be considered accurate only if any tensile normal stresses are proved to be negligible, a point which will be addressed subsequently.

The procedure for solving (14) with conditions (15) and (16) is involved and utilizes both analytical and numerical integration techniques. Our method, discussed in detail in the Appendix, is similar to the approach taken by Thouless *et al.* (1987) to solve the pair of equations (11), (12) governing the response to a compressive end stress.

2.1. *Analytical results*

To test the accuracy of our model, we first generalized the numerical procedure described in the appendix for solution of the set of equations (11), (12) governing the response to an applied remote compression and compared model predictions with the results of Thouless *et al.* (1987). Predictions of the stress intensity factors K_I and K_{II} obtained using our method and the somewhat different method used in Thouless *et al.* are virtually identical.

We then proceeded to solve the problem described in Fig. 3(c) for the case of no frictional interaction across the interface ($\mu_f = 0$). The calculated dislocation density, normalized by the misfit strain, β_x/ε_0, is plotted versus the normalized distance from the crack tip, x/h, in Fig. 5.

In the absence of friction, an exact result for the energy release rate, which we denote as G^0, is easily obtained using simple energy arguments (Rice, 1968; Eshelby, 1974; Kendall, 1978). These require that, in the absence of interfacial friction, the energy release rate G^0 is $\varepsilon_0\sigma_0 h/2$, so that $G^0/(E'\varepsilon_0^2 h) = 1/2$. Similarly, the corresponding mode II stress intensity factor $K_{II}^0 = \sqrt{E'G^0}$, so that $K_{II}^0/(\sigma_0\sqrt{h})$ is $\sqrt{2}/2$.

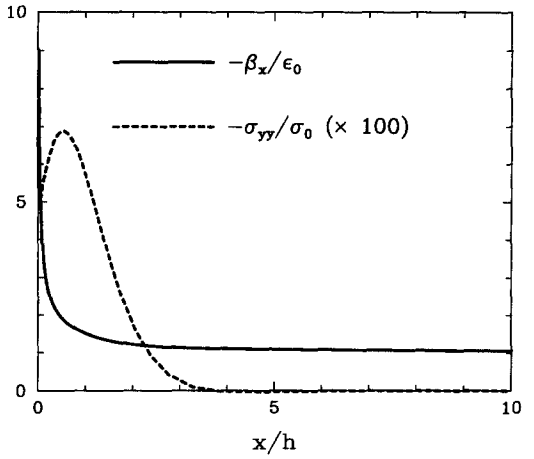

Fig. 5. Analytical predictions of dislocation density distribution and normal stress distribution for the case of no friction.

Using the relationship

$$K_{II} = \lim_{x \to 0} \frac{\sqrt{2\pi E' x}}{4} \beta_x, \tag{17}$$

we calculated K_{II} based upon our solution for β_x. As discussed in the Appendix, when deriving the solution to (14), we varied both the number of locations at which these equations were evaluated (N) and the number of stations used in the numerical integration scheme (M) until the error between the predicted value of K_{II} and the exact value, $K_{II}^0 = \sqrt{2/2}\sigma_0\sqrt{h}$, were sufficiently small. For $N = 16$, $M = 400$, our calculations indicate that $K_{II}/K_{II}^0 = 1.002$, and for $N = 64$, $M = 1000$, we find that $K_{II}/K_{II}^E = 1.001$.

The calculated normal stress distribution, normalized by the remote stress σ_{yy}/σ_0, is also plotted versus x/h in Fig. 5. As indicated in the figure, σ_{yy} is non-zero over a distance of only about three film thicknesses from the crack tip. The peak stress occurs at $x/h \approx 1/2$, and has a magnitude of only about 7% of the remote tensile load. It then drops to about 5% of σ_0 at the crack tip.

As discussed earlier, these calculations were made under the assumption that contact occurs over the entire length of the crack, so that $\beta_y = 0$. Since, however, we did not impose any restrictions on σ_{yy}, our approximate solutions generally produced small positive values for σ_{yy} at large values of x. The maximum calculated tensile stress was less than 0.7% of the maximum compressive stress, and the presence of tensile stress is barely noticeable in Fig. 5. We thus feel confident that the assumption that $\beta_y = 0$ is not a source of significant error.

We next consider the effects of local interfacial Coulomb friction acting behind the delamination front, with μ_f varying between zero and one. In experiments performed on the sliding of gold on glass, Kim (1991) measured coefficients of interfacial sliding friction in the range 0.9–1.2.

In arriving at an accurate solution to (14), it was necessary to determine the nodal locations for which the predicted values of σ_{yy} were tensile so that σ_{xy} could be set to zero for these points. We therefore solved (14) using an iterative scheme in which we first estimated σ_{yy} based upon its value at some smaller value of μ_f. Using the estimated value of σ_{yy}, we then solved for β_x at the N nodal locations, producing a new estimate of σ_{yy}. We iterated this procedure until each nodal prediction of σ_{yy} did not change with respect to its value at the previous increment. Because the calculated tensile stresses were so small, only a few iterations were required for each case.

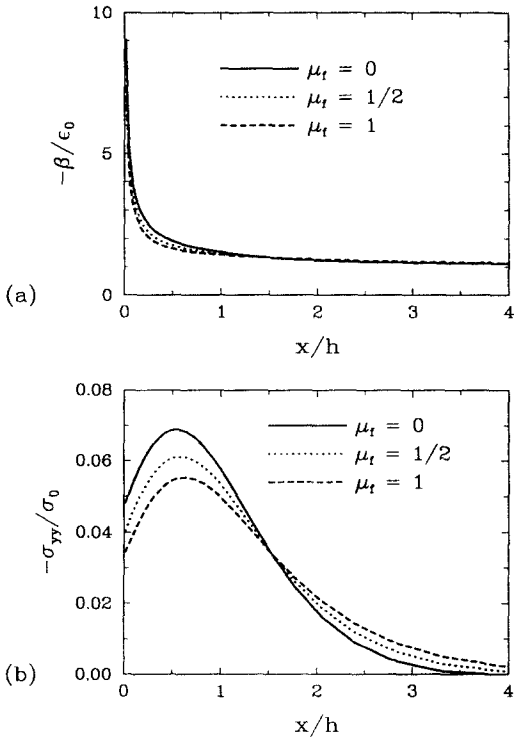

Fig. 6. Results of the exact analysis for $\mu_f = 0$, $\mu_f = 1/2$ and $\mu_f = 1$. (a) Dislocation density distributions. (b) Normal stress distributions.

Figure 6 shows the effect of local friction on the dislocation density and the normal stress distribution for $\mu_f = 0$, $\mu_f = 1/2$ and $\mu_f = 1$. As indicated in the figure, β_x decreases with increasing μ_f, but the effect is very local to the crack tip. The contact stress σ_{yy} decreases more substantially with increasing μ_f. The distribution of σ_{yy} also becomes noticeably more diffuse. Although the resulting shear stress σ_{xy} is quite small relative to the magnitude of the remote stress σ_0, its effect on the stress intensity factor is significant. Model predictions of K_{II}/K_{II}^0 are shown in Fig. 7(a) together with a result derived from an edge crack solution, discussed in the paragraph to follow. For a friction coefficient of $\mu_f = 1$, our calculations indicate that there is about a 19% decrease in the stress intensity factor K_{II}, or a 35% decrease in the energy release rate G with respect to the respective corresponding exact values in the absence of friction, K_{II}^0 and G^0. Note that as μ_f increases, the *rate of decrease* in K_{II} becomes smaller.

The significant drop in the stress intensity factor caused by the relatively small frictional resistance can be qualitatively verified using standard solutions for the stress intensity factor. According to Tada *et al.* (1973), the stress intensity factor for an edge crack with a pair of opposing concentrated loads of magnitude Q acting on the crack faces a distance d behind the crack tip and oriented parallel to the crack plane [Fig. 7(b)] is given by

$$K_{II} = \frac{2Q}{\sqrt{2\pi d}}. \tag{18}$$

For a distribution of shear stress $\sigma_{xy}(s)$, the corresponding stress intensity factor is

$$K_{II} = \frac{2}{\sqrt{2\pi}} \int_0^\infty \frac{\sigma_{xy}(s)}{\sqrt{s}} \, ds. \tag{19}$$

Predictions for K_{II} obtained by subtracting the solution obtained using (19) with the calculated $\sigma_{xy}(s)$ from K_{II}^0 are given for comparison in Fig. 7(a) and indicate that model

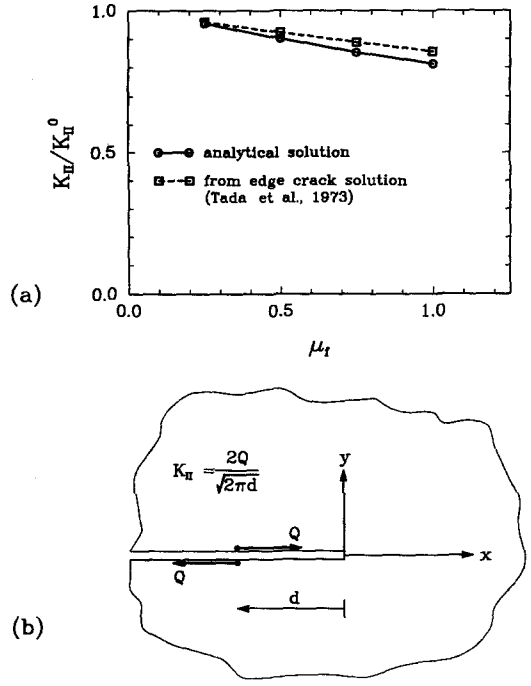

Fig. 7. (a) A comparison of analytical model predictions for the stress intensity factor with results obtained using edge crack solution (Tada *et al.*, 1973) and calculated contact stress distribution. (b) Diagram of edge crack solution for a pair of point forces oriented as indicated.

predictions of K_{II} are reasonable. Differences can be attributed to the fact that (19) is based upon the assumption that the body is infinite in extent, whereas in our problem there is a free surface near the crack plane.

3. A MORE GENERAL NUMERICAL MODEL

The analytical model proposed in the previous section can be applied only to the simplest material and loading combinations, namely, a film and substrate with identical elastic properties and no remote applied bending load. In this section we describe the finite element method that we used in order to extend the central idea to the important cases in which (a) the material properties of the film and substrate are different, and (b) the remote bending and in-plane loads arising from the post-buckling response of the film are taken into account.

Figure 8 depicts the finite element model used for this purpose. A large number of elements is required to capture the local effects of friction and at the same time to approximate the infinite extent of the half-plane. The geometry of the elements surrounding the crack tip was designed so that nodal locations were optimum for simulation of the singular behavior of the fields near the tip. We used version 4.8 of the ABAQUS finite element code (Hibbitt, Karlsson and Sorensen, Inc., 1990). The mesh shown in Fig. 8 has 650 eight-node plane strain isoparametric (CPE8) elements of which 480 are located in the indicated region near the crack tip. Interface elements (INTER3) were used to model the debonded interface between the film and the substrate. These elements allow for contact when normal stresses are compressive and separation when normal stresses are tensile. Frictional properties can be added to these elements. A tensile stress was applied to the face of the film elements at $+x_\infty$. The nodes along $-x_\infty$ were constrained to have zero displacement in the x-direction while the nodes along $-y_\infty$ were constrained to have zero displacement in the y-direction.

In order to assess the accuracy of the numerical approach, we first considered the problem that we previously solved analytically. We performed calculations for three cases: $\mu_f = 0$, $\mu_f = 1/2$ and $\mu_f = 1$. The agreement between numerical and analytical predictions of

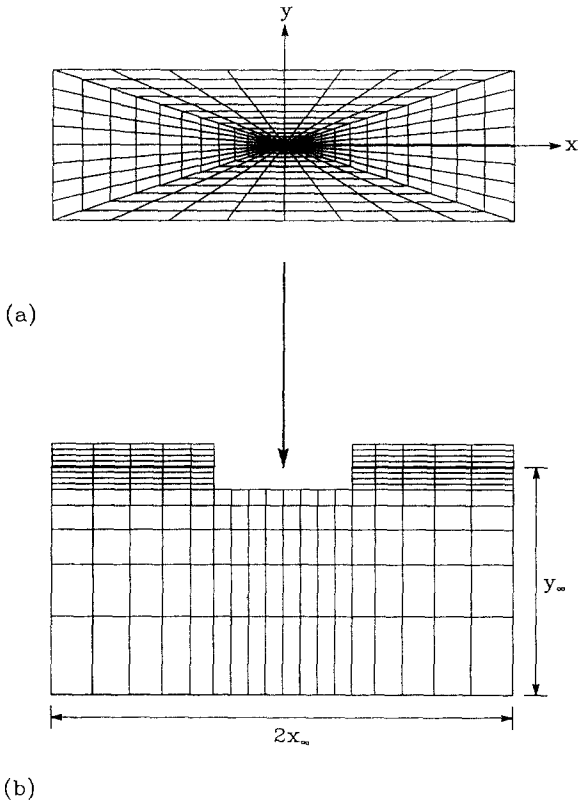

Fig. 8. The finite element mesh. The grid at the top fits into the grid at the bottom as indicated. The thick horizontal line indicates the interface elements.

β_x and σ_{yy} is excellent. A comparison of finite element and model predictions for β_x and σ_{yy} is shown for the $\mu_f = 1$ case in Fig. 9.

It is well known that the prediction of stress intensity factors using nodal displacements is not very accurate. We therefore used the J-integral evaluation procedure of ABAQUS to calculate G. Due to the numerical nature of the finite element method, the J-integral is not entirely path-independent even in the absence of friction, nonetheless, for $\mu_f = 0$ we found that the difference between J values calculated along successive contours through concentric rings of elements surrounding the crack tip differed by less than 0.2%. We further observed that the discrete nature of the finite element mesh led to errors in G that decreased

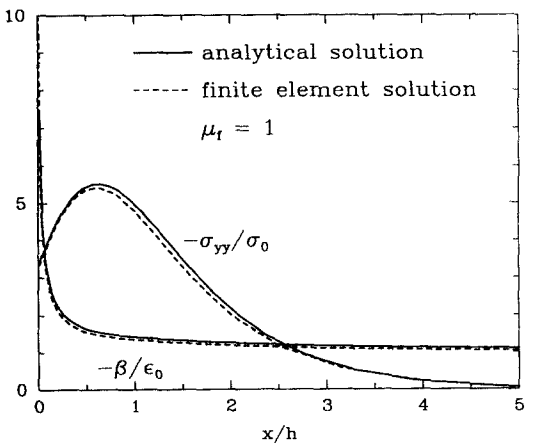

Fig. 9. A comparison of analytical and finite-element predictions of the dislocation density and normal stress distributions for $\mu_f = 1$.

Table 1. Comparison of analytical and numerical predictions of K_{II}/K_{II}^0 for $\mu_f = 0$, $\mu_f = 1/2$ and $\mu_f = 1$.

	$\mu_f = 0$	$\mu_f = 1/2$	$\mu_f = 1$
Analytical	1.0001	0.9011	0.8134
Numerical	0.9990	0.9081	0.8223

as the extent of the mesh in the x-direction, x_∞, increased. For example, for $\mu_f = 0$, our calculations indicate that for $x_\infty = 100$, $G/G^0 = 0.992$ whereas for $x_\infty = 1000$, $G/G^0 = 0.999$. The results were much less sensitive to variations in y_∞, which we set equal to 100. We further found that using the contour through the innermost ring of elements provided the most accurate prediction of G. We subsequently used the innermost contour for determining G (and K_{II}) for all other cases. When calculated in this manner, we found excellent agreement between analytical and numerical predictions of G, as summarized in Table 1.

We next considered several cases for which the elastic compliances of the film and the substrate were different. In particular, keeping the elastic modulus of the film, E_f, constant so that the reference energy release rate, G^0, would not change, we varied the ratio of the elastic modulus of the substrate, E_s, to that of the film from 1/4 to 4, by factors of 2. We again considered three friction coefficients: 0, 1/2 and 1.

Model predictions of σ_{yy}/σ_0 versus x/h are shown in Fig. 10 for $\mu_f = 0$ and for $\mu_f = 1$. From this figure, one can infer that systems with more compliant films ($E_f < E_s$) generate higher local contact stresses relative to the remotely applied stress, σ_0. As E_f/E_s increases, the crack tip value of σ_{yy}/σ_0 becomes progressively smaller until, when the substrate becomes more compliant than the film, separation occurs close to the crack tip. For these compliant substrates, contact does eventually occur further away from the crack tip, but the stresses are substantially reduced. The corresponding predictions of the normalized energy release rate, shown in Fig. 11, as expected, show that frictional resistance is much larger for stiff substrates and can lead to reductions in the energy release rate of up to 55% ($G/G^0 = 0.45$) within the given range of relative compliance ratios. Note that G should not be affected by compliance differences when $\mu_f = 0$, so that the solid curve in Fig. 11 gives some sense of the quality of the finite element calculations. Further calculations indicate that G/G^0 levels off at about 0.4 for extremely stiff substrates.

Finally, we considered the additional effects of the moment and in-plane forces that arise during the post-buckling response of the film. These effects are expected to be significant only for relatively small delaminations, measured in terms of $\sqrt{\varepsilon_0}b/h$, where the length of the delamination is $2b$ [see Fig. 2(a)]. The post-buckling moment and in-plane

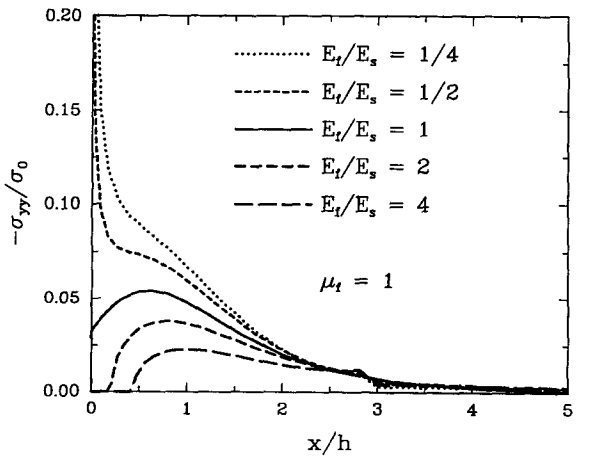

Fig. 10. Finite element predictions of the normal stress distribution for various material stiffness combinations, $\mu_f = 1$.

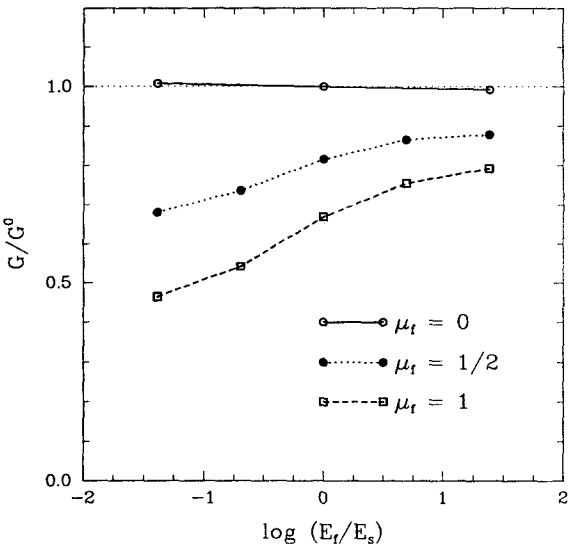

Fig. 11. Finite element predictions of the normalized energy release rate, G/G^0, for various material stiffness combinations and friction coefficients.

force can be estimated using the solution for buckling of a fully clamped plate. The solution to this problem is well known and is given, for example, in Chai *et al.* (1981) or Hutchinson and Suo (1990). The critical buckling stress, σ_c, is found to be

$$\sigma_c = \frac{\pi^2}{12} E_f' \left(\frac{h}{b}\right)^2, \tag{20}$$

where $E_f' = E_f/(1-\nu_f^2)$. The moment, M_{zz}, and in-plane force, N_x, per unit width are then given as

$$M_{zz} = \frac{\pi^2}{24} E_f' \left(\frac{h}{b}\right)^2 h^2 \eta, \tag{21}$$

$$N_x = \frac{\pi^2}{16} E_f' \left(\frac{h}{b}\right)^2 h\eta^2 - \sigma_0 h, \tag{22}$$

where

$$\eta = \left[\frac{4}{3}\left(\frac{\sigma_0}{\sigma_c} - 1\right)\right]^{1/2}. \tag{23}$$

Normalizing M_{zz} by $\frac{1}{2}\sigma_0 h^2$, the closing moment per unit width due to the remote stress field σ, normalizing N_x by $\sigma_0 h$, the remote in-plane force, and substituting for η and σ_c, we find that

$$\frac{M_{zz}}{\frac{1}{2}\sigma_0 h^2} = \frac{2}{\sqrt{3}} \frac{\sqrt{\theta - 1}}{\theta}, \tag{24}$$

$$\frac{N_x}{\sigma_0 h} = -\frac{1}{\theta}, \tag{25}$$

where

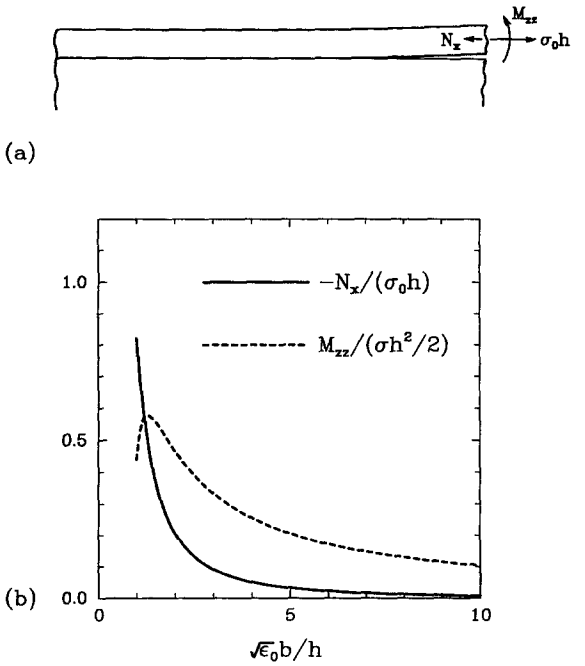

Fig. 12. (a) A diagram showing the orientation of the post-buckling bending moment, M_{zz} and in-plane force, N_x. (b) $M_{zz}/(\frac{1}{2}\sigma_0 h^2)$ and $N_x/(\sigma_0 h)$ as functions of $\sqrt{\varepsilon_0} b/h$.

$$\theta = \frac{\sigma_0}{\sigma_c} = 12\varepsilon_0\left(\frac{b}{\pi h}\right)^2. \tag{26}$$

The presence of an in-plane force has the effect of reducing the remote tensile load of Fig. 3(c), while the bending moment tends to lift the film from the substrate, as shown in Fig. 12(a). According to (24) and (25), the moment and in-plane force indeed become much smaller as b/h increases. Calculated values of $M_{zz}/(\frac{1}{2}\sigma_0 h^2)$ and $N_x/(\sigma_0 h)$ are plotted versus $\sqrt{\varepsilon_0} b/h = \pi\theta/\sqrt{12}$ in Fig. 12(b).

For our finite element study of the effects of bending moment, we considered several values of $\sqrt{\varepsilon_0} b/h$ in the range 2–20, with $\mu_f = 1$ and $E_f' = E_s'$. (The results presented earlier in this section represent the limiting case, $\sqrt{\varepsilon_0} b/h \to \infty$.)

Predictions of σ_{yy}/σ_0 versus x/h for several values of $\sqrt{\varepsilon_0} b/h$ are shown in Fig. 13(a). As $\sqrt{\varepsilon_0} b/h$ decreases, the increasing bending moment pushes the region of contact progressively toward the delamination front. For values of $\sqrt{\varepsilon_0} b/h > 5$, there is an accompanying increase in the magnitude of σ_{yy}. However, as $\sqrt{\varepsilon_0} b/h$ decreases below about five, σ_{yy} begins to decrease as well.

The effect of moment on the energy release rate is depicted in Fig. 13(b), where we have plotted G/G^* versus $h/(\sqrt{\varepsilon_0} b)$; G^* is a quantity analogous to G^0 representing an exact value of G for $\mu_f = 0$ and $E_f' = E_s'$ in the presence of a bending moment, and is given as

$$G^* = \frac{(\sigma_0 h + N_x)^2 + 12(M_{zz}/h)^2}{2E_f' h}. \tag{27}$$

The variation of G/G^* with $h/(\sqrt{\varepsilon_0} b)$ is consistent with the calculated values of contact stress shown in Fig. 13(a). For $\sqrt{\varepsilon_0} b/h > 5$ ($h/\sqrt{\varepsilon_0} b < 0.2$), because the magnitude of σ_{yy} increases as the contact zone decreases, the total frictional resistance remains relatively constant; G/G^* in fact decreases slightly. Then, as $\sqrt{\varepsilon_0} b/h \to 2$, G/G^* approaches unity, indicating that the sizable moment has caused the film to completely separate from the substrate.

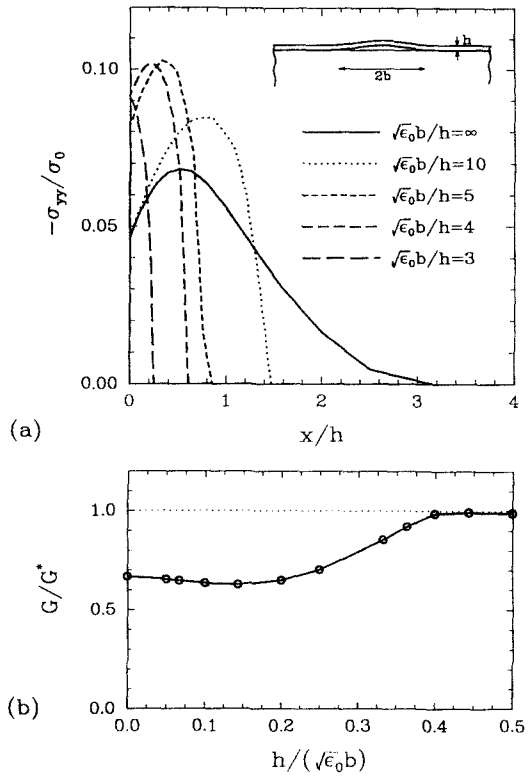

Fig. 13. (a) Finite element predictions of σ_{yy}/σ_0 for various values of $\sqrt{\varepsilon_0}b/h$. (b) Predictions of G/G^* as a function of $h/(\sqrt{\varepsilon_0}b)$.

4. SUMMARY

The results presented in the previous sections clearly show that frictional resistance contributes to much of the observed toughness increase accompanying a shift in the phase angle below $\psi = 90^\circ$ for "pure mode II" loading. To illustrate this point, we reconsider the toughness versus phase angle curve presented in Fig. 1. For a material combination with a stiffness ratio between the film and the substrate equal to or greater than four, our calculations indicate that 55–60% of the fracture resistance can be attributed to friction. The interpretation of this curve clearly changes for phase angles less than $\psi = -90^\circ$, as was anticipated at the outset of this analysis.

The results presented in the previous section are particularly significant in light of the emergence of highly compliant film materials such as polyimide. Based upon the results presented here, it seems likely that polyimide and other highly compliant materials will exhibit excellent interfacial toughness properties in combination with many substrate materials when in residual compression.

The quantification of the frictional contribution to mode II interfacial toughness may prove useful not only in the design of interfacial properties which take advantage of these results, but also for determining resistance to interfacial fracture in cases where frictional effects are not present, such as when the interface is pressurized. At the very least, a reinterpretation of existing toughness data seems warranted.

Given the magnitude of frictional effects, experiments aimed at verifying these results and measuring coefficients of friction for various systems would seem to represent an important direction for future investigations.

Acknowledgements—This work was supported by Office of Naval Research Contract N00014-90-J-4051 with Brown University and by an IBM Research Award in Materials Science.

REFERENCES

Chai, H., Babcock, C. D. and Knauss, W. G. (1981). One dimensional modelling of failure in laminated plates by delamination buckling. *Int. J. Solids Structures* **17**, 1069–1083.

Dundurs, J. (1969). Elastic interaction of dislocations with inhomogeneities. In *Mathematical Theory of Dislocations* (Edited by T. Mura), pp. 70–115. ASME, New York.
Erdogan, F., Gupta, G. D. and Cook, T. S. (1973). Numerical solution of singular equations. In *Mechanics of Fracture I: Methods of Analysis and Solution of Crack Problems* (Edited by G. C. Sih), pp. 368–425. Noordhoff, The Netherlands.
Eshelby, J. D. (1974). The calculation of energy release rates. In *Prospects in Fracture Mechanics* (Edited by G. C. Sih), pp. 69–83. Noordhoff, The Netherlands.
Evans, A. G. and Hutchinson, J. W. (1984). On the mechanics of delamination and spalling in compressed films. *Int. J. Solids Structures* **20**, 455–466.
Head, A. K. (1953). Edge dislocations in inhomogeneous media. *Phil. Mag.* **44**, 793–801.
Hibbitt, Karlsson and Sorensen, Inc. (1990). ABAQUS version 4.8, Providence, RI.
Hutchinson, J. W. and Suo, Z. (1991). Mixed mode cracking in layered materials. In *Advances in Applied Mechanics* (Edited by J. W. Hutchinson and T. Y. Wu), Vol. 29, pp. 63–191, Academic Press, San Diego.
Kendall, K. (1978). The complexities of compression failure. *Proc. R. Soc.* **A361**, 245–263.
Kim, K. S. (1991). Private communication.
Liebfried, G. (1951). Verteilung von versetzungen im statischen gleichgewicht. *Z. Phys.* **130**, 214–226.
Rice, J. R. (1968). A path independent integral and the approximate analysis of strain concentration by notches and cracks. *J. Appl. Mech.* **35**, 379–386.
Tada, H. Paris, P. and Irwin, G. (1973). *The Stress Analysis of Cracks Handbook*. Del Research Corporation, Hellertown, PA.
Thouless, M. D., Evans, A. G., Ashby, M. F. and Hutchinson, J. W. (1987). The edge cracking and spalling of brittle plates. *Acta Metall.* **35**, 1333–1341.
Whitcomb, J. D. (1986). A parametric analytical study of instability related delamination growth. *Compos. Sci. Technol.* **25**, 19–48.

APPENDIX

Solution procedure

In this appendix, we describe the numerical procedure used to solve the singular integral equation (14) governing the response of the system shown in Fig. 3(c) to a remote tensile load, for which contact occurs between the film and the substrate. We note that a tensile load applied remotely to the film corresponds, through the superposition scheme outlined in Fig. 3, to the case of residual compression in the film.

We first perform a change of variables in order to obtain a finite domain of integration. Let $x = (1+z)/(1-z)$ and $s = (1+t)/(1-t)$. Then $ds = 2/(1-t)^2$ and $1/(x-s) = (1-z)(1-t)/2(z-t)$. Substituting for x, s and ds in (11) and (12) and setting β_y to zero, we have

$$\sigma_{xy} = \frac{\mu}{4\pi(1-\nu)}\int_{-1}^{1} \frac{g_{11}(z-t)(1-z)\bar{\beta}(t)}{(z-t)(1-t)}\,dt, \tag{A1}$$

$$\sigma_{yy} = \frac{\mu}{2\pi(1-\nu)}\int_{-1}^{1} \frac{g_{21}(z-t)\bar{\beta}(t)}{(1-t)^2}\,dt, \tag{A2}$$

where

$$\bar{\beta}(t) = \beta_x\left(\frac{1+t}{1-t}\right). \tag{A3}$$

The condition (15) that far away from the delamination front the film is in a state of constant plane strain tension with a prescribed tension σ_0, is now written as

$$\lim_{t\to 1}\bar{\beta}(t) = \varepsilon_0 = \frac{1-\nu^2}{E}\sigma_0. \tag{A4}$$

Similarly, the square-root singularity condition (16) near the delamination front becomes

$$\lim_{t\to -1}\bar{\beta}(t) \propto \frac{1}{\sqrt{1+t}}. \tag{A5}$$

Standard techniques for solution of singular integral equations, such as the Muskhelishvili methods employed by Erdogan *et al.* (1973), are not appropriate when the unknown quantity is square-root singular at one endpoint and is a nonzero constant at the other. We therefore use an ad hoc procedure to solve (14).

Let the dislocation density $\bar{\beta}$ have the following form:

$$\bar{\beta}(t) = \frac{1}{\sqrt{1+t}}\left[a_0 + (1-t)\sum_{n=1}^{N} a_n t^{n-1}\right]. \tag{A6}$$

Thouless *et al.* (1987) chose a similar form for β_x and β_y in their model, differing only in their use of Tchebychev polynomials, $T_n(t)$, rather than the simple polynomials t^{n-1} used in (A6). Given the ad hoc nature of the integration procedures, it is not clear that they gained any advantage by using this more complex polynomial. It can easily be seen that the form of $\bar{\beta}$ given in (A6) satisfies the endpoint requirements (A3) and (A4). From condition (A4), it can be shown that $a_0 = \sqrt{2}\varepsilon_0$. We therefore must determine the remaining coefficients a_n.

Substituting for $\bar{\beta}$ from (A6) into (A2) and setting $\sigma_{xy} = -\mu_f \sigma_{yy}$, we have

$$\int_{-1}^{1} \frac{g_{11}(z-t)(1-z)\left[a_0+(1-t)\sum_{n=1}^{N} a_n t^{n-1}\right]}{(z-t)(1-t)\sqrt{1+t}}\,dt = -2\mu_f \int_{-1}^{1} \frac{g_{12}(z-t)\left[a_0+(1-t)\sum_{n=1}^{N} a_n t^{n-1}\right]}{(1-t)^2\sqrt{1+t}}\,dt. \tag{A7}$$

Each integral in (A7) is singular at $z = -1$. The integral on the left-hand side of (A7) is also singular at $z = t$. Neither integral is singular at $z = 1$ because g_{11} and g_{12} approach zero rapidly as $z \to 1$.

Each term in the singular integral on the left-hand side of (A7) is of the form

$$I_p = \int_{-1}^{1} \frac{f(z,t)}{z-t}\frac{1-z}{1-t}\frac{t^p}{\sqrt{1+t}}\,dt. \tag{A8}$$

We can isolate the $1/(z-t)$ singularity by noting that (A8) can be expressed in the following form:

$$I_p = \int_{-1}^{1} \frac{t^p}{(t-z)\sqrt{1+t}}\,dt + \int_{-1}^{1} \frac{t^p}{(t-z)\sqrt{1+t}}\left[f(z,t)\frac{1-z}{1-t}-1\right]dt. \tag{A9}$$

Only the first of these two integrals is singular at $z = t$.

The $1/\sqrt{1+t}$ singularity in each term of (A7) must also be removed. We accomplish this through a second change of variables: $t = u^2 - 1$, $dt = 2u\,du$; (A9) can now be rewritten as

$$I_p = \int_0^{\sqrt{2}} \frac{(u^2-1)^p}{u^2-(1+z)}\,du + \int_0^{\sqrt{2}} \frac{(u^2-1)^p}{u^2-(1+z)}\left[f(z,u)\frac{1-z}{-u^2}-1\right]du. \tag{A10}$$

The singular integral first term of (A10) can be evaluated analytically. Using a binomial expansion,

$$(u^2-1)^p \approx (-1)^p\left[1-pu^2+\frac{p(p-1)}{2!}u^4-\frac{p(p-1)(p-2)}{3!}u^6+\cdots\right]. \tag{A11}$$

Thus, we must evaluate terms of the form

$$I_q = \int_0^{\sqrt{2}} \frac{u^{2q}}{u^2-(1+z)}\,du, \tag{A12}$$

where q varies from 0 to p.

Through integration by parts, it can be shown that

$$\int_0^c \frac{u^{2q}}{u^2-d^2}\,du = \sum_{r=1}^{q} \frac{c^{(2r-1)}d^{2(q-r)}}{2r-1} + \frac{1}{2}d^{(2q-1)}\log\left[\frac{c-d}{c+d}\right]. \tag{A13}$$

Thus, after some manipulation,

$$I_p = (-1)^p \sum_{q=0}^{p} c_q\left\{\sum_{r=1}^{q} \frac{2^{(r+1/2)}(1+z)^{(q-r)}}{2r-1} + (1+z)^{(q-1/2)}\log\left[\frac{\sqrt{2}-\sqrt{1+z}}{\sqrt{2}+\sqrt{1+z}}\right]\right\}, \tag{A14}$$

where

$$c_q = (-1)^q \frac{\prod_{l=0}^{k-1}(p-j)}{q!}, \quad q \geqslant 1,$$

$$c_0 = 1. \tag{A15}$$

The second term in each of (A7) and (A10) must be evaluated numerically. We used a Gauss–Legendre numerical integration scheme, for which

$$\int_0^{\sqrt{2}} f(u)\,du \approx \sum_{m=1}^{M} f(u)_m w_m, \tag{A16}$$

where u_m is the mth location in the interval $[0, \sqrt{2}]$ at which the function $f(u)$ is evaluated and w_m is the corresponding weight assigned to each contribution $f(u_m)$ to the sum.

To determine the N coefficients a_n appearing in (A7), we evaluate the equation at N locations z_n in the interval $[-1, 1]$. Since $a_0 = \sqrt{2}\varepsilon_0$ is known, we move its contribution to the integral to the right-hand side of the equation. In this manner, we arrive at an N by N system of equations

$$\sum_{k=1}^{N} A_{jk}a_k = B_j, \tag{A17}$$

Table A1. Results of convergence study

N \ M	10	40	100	400	1000	4000
1	1.116	1.126	1.126	1.126	1.126	1.216
2	0.9996	0.9995	0.9995	0.9995	0.9995	0.9995
4	0.9704	0.9626	0.9626	0.9626	0.9626	0.9626
8	0.6862	1.008	0.9988	0.9989	0.9989	0.9989
16	−0.0010	0.5487	0.9814	1.0023	1.0023	1.0023
32	−0.1115	0.8976	1.655	1.0025	1.0025	1.0025
64	−0.4528	−0.6104	0.2602	0.9139	1.0012	1.0011

with

$$A_{jk} = \sum_{m=1}^{M} \left\{ \left[\frac{g_{11}(z_j, u_m)(1-z_j)-1}{z_j - t_m} \right] + 2\langle \mu_f \rangle \frac{g_{12}(z_j, s_m)}{1-t_m} \right\} \frac{u_m w_m t_m^{k-1}}{\sqrt{1+t_m}} + \sum_{q=0}^{k} c_q \left\{ \sum_{r=1}^{q} \frac{2^{(r+1/2)}(1+z_j)^{(q-r)}}{2r-1} + (1+z_j)^{(q-1/2)} \log \left[\frac{\sqrt{2}-\sqrt{1+z_j}}{\sqrt{2}+\sqrt{1+z_j}} \right] \right\} \quad \text{(A18)}$$

and

$$B_j = \sum_{m=1}^{M} \left\{ \left[\frac{g_{11}(z_j, u_m)\dfrac{1-z_j}{1-t_m} - 1}{z_j - t_m} \right] + 2\langle \mu_f \rangle \frac{g_{12}(z_j, u_m)}{(1-t_m)^2} \right\} \frac{u_m w_m}{\sqrt{1+t_m}} + (1+z_j)^{(1/2)} \log \left[\frac{\sqrt{2}-\sqrt{1+z_j}}{\sqrt{2}+\sqrt{1+z_j}} \right]. \quad \text{(A19)}$$

Here the function $\langle \mu_f \rangle$ is defined such that

$$\langle \mu_f \rangle = \begin{cases} \mu_f & \text{if } \sigma_{yy} < 0, \\ 0 & \text{if } \sigma_{yy} \geqslant 0. \end{cases} \quad \text{(A20)}$$

We found that optimal results are obtained by using N nodes v_k that are equally spaced in the interval $[0, \sqrt{2}]$, so that the z_k in (A18) and (A19) are given by $z_k = v_k^2 - 1$. Because we have compressed the domain of integration, the functions g_{11} and g_{12} are not well behaved for large values of x, and it is extremely difficult to accurately evaluate the integrals for these nodes. We therefore found that convergence was very slow and nonuniform, in the sense that an increase in the number of nodes N did not always lead to smaller numerical errors. We also found that the number of terms in the Gauss–Legendre integration scheme, M, must be very large in order to accurately evaluate the integrals when N is large. This can be traced to the fact that, as N increases, the integrals must be evaluated for successively larger values of x. Thus the increased accuracy brought about by using more nodes is offset to a large extent by the less accurate numerical evaluation of the integrals. A summary of our convergence study is given in Table A1.